Effects of Co and Ru Intimacy in Fischer−Tropsch Catalysts Using Hollow Carbon Sphere Supports: Assessment of the Hydrogen Spillover Processes

Tumelo N. Phaahlamohlaka,[†,‡] David O. Kumi,[†] Mbongiseni W. Dlamini,[†,‡] Roy Forbes,[†] Linda L. Jewell,[§,‡] David G. Billing,[†,⊥] and Neil J. Coville*[,†,‡]

[†]Molecular Sciences Institute, School of Chemistry, University of the Witwatersrand, Johannesburg 2050, South Africa

[§]Department of Chemical Engineering, University of South Africa, Private Bag X6, Florida 1710, South Africa

[‡]DST-NRF Centre of Excellence in Catalysis (c*change), Rondebosch 7701 South Africa

[⊥]DST-NRF Centre of Excellence in Strong Materials, Johannesburg 2050, South Africa

*   Supporting Information

ABSTRACT: Mesoporous hollow carbon spheres (MHCSs) were synthesized (d = 290 nm; carbon shell 20−35 nm), and their hollow morphology was exploited to study the influence of Ru nanoparticle location relative to Co_3O_4 nanoparticles on the reduction behavior and activity of Co Fischer−Tropsch catalysts. Ru nanoparticles were loaded both inside and outside the MHCS, while Co_3O_4 particles (ca. Co 15 wt % loading) were loaded on the outside of the MHCS. The use of in situ powder X-ray diffraction (PXRD) and temperature-pro-grammed reduction studies on the catalysts indicated the effect of Ru location on the Co_3O_4 reduction pathways. A secondary hydrogen spillover effect was invoked to explain a

complete reduction of the Co_3O_4 on Ru@MHCS@Co at 450 °C. Secondary hydrogen spillover enhanced the CoO to Co transformation by lowering the reduction temperature when compared to the unpromoted catalyst. Primary hydrogen spillover was inferred to explain the complete reduction of Co_3O_4 to Co metal on CoRu/MHCS at 300 °C. After catalyst activation at 350 °C, the primary spillover process yielded a catalyst with higher Fischer−Tropsch activity (ca. 2×) than the unpromoted catalyst and the catalysts where Ru and Co were separated by the mesoporous carbon shell. This was partially related to the Co phases that formed on the carbon support during reduction and the catalyst degree of reduction that was reliant on the type of hydrogen spillover process.

KEYWORDS: ruthenium, hydrogen spillover, reduction, hollow carbon spheres, Fischer−Tropsch synthesis, in situ powder X-ray diffraction (PXRD)
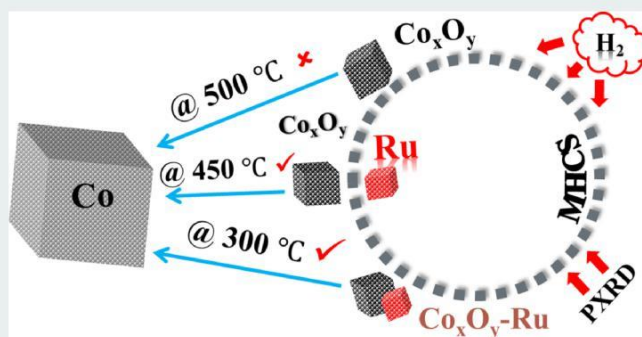
1. INTRODUCTION

Cobalt Fischer−Tropsch synthesis (FTS) catalysts are generally promoted with metals such as ruthenium, platinum, and rhenium in order to enhance the catalytic activity of the cobalt active sites.[1−3] This is believed to occur by a promotion effect in which the added metal assists in lowering the reduction temperatures of the cobalt oxide. The promoter metals are able to dissociate hydrogen gas at lower temperatures and thus lower the reduction temperature of cobalt oxide nanoparticles in comparison to unpromoted catalysts.[4−7] The reducibility of cobalt oxide particles is especially lowered if oxidic supports such as titania and alumina are used. This is due to the increased metal−support interaction (MSI) that makes reduction of the Co_xO_y more difficult, hence the need for reduction promoters.[1,8] These reduction promoters can be classified as electronic promoters since they affect the electronic structure of cobalt particles and they in turn have a significant

bearing on the overall cobalt catalytic activity and selectivity.[9] The promotion effects, as in many catalytic systems, are dependent on the intimacy (proximity) of the different catalyst components. A case in point is the use of bifunctional catalysts for the hydrocracking of long chain hydrocarbons where the location of the acid and metal sites play a crucial role in the reaction.[10]

In promoted Co catalysts, the cobalt oxide crystallites can be in direct or indirect contact with a promoter,[11] hence several mechanisms to explain the promotion effect of noble metals on the cobalt oxide particles have been proposed.[3,12] One of these involves hydrogen spillover in which a noble metal not only serves as a reduction promoter for the metal oxide (i.e., cobalt

1

oxide) but also plays a role in the reaction selectivity.[6,7] Two types of hydrogen spillover processes can be envisaged (see Scheme 1): (1) a primary hydrogen spillover, whereby the

Scheme 1. Hydrogen Spillover Pathways, (a) Primary and (b) Secondary[a]
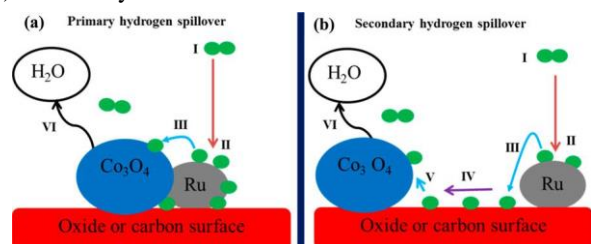
[a]I, Molecular hydrogen; II, dissociative adsorption; III, spillover; IV, hydrogen atom surface migration; V, spillover; VI, reduction and water removal. Adapted from refs 12 and 14.

promoter (i.e., initiator) is in contact with the cobalt oxide (i.e., acceptor) and dissociated hydrogen atoms can move from the initiator directly to the acceptor, and (2) a secondary hydrogen spillover, in which the initiator and the acceptor materials are separated by some distance and migration of the atomic hydrogen occurs from the initiator to the acceptor via a carrier (or catalyst support).[12−14]

Hydrogen spillover on Fischer−Tropsch catalysts has been typically studied using hybrid catalysts composed of a mechanical mixture of the supported initiator and acceptor.[6,7,15]

The hydrogen spillover and the mobility of the spilled-over hydrogen have been suggested to occur over long distances (up to several millimeters). The effects of such long-range migration of hydrogen may be very small and may not be revealed in Fischer−Tropsch reactions.[6] Hydrogen spillover studies involving Co Fischer−Tropsch catalysts have generally been performed on oxidic supports and were observed to offer a limited hydrogen spillover effect over long hydrogen transfer distances. A literature survey by Prins suggests that, in principle, hydrogen spillover on defective materials such as carbon nanomaterials is viable.[14] This is because hydrogen can be chemically adsorbed on the carbon defect sites, which are generally present on nongraphitic carbons. As with oxidic carriers heteroatoms such as oxygen or nitrogen also enhance the ability of carbon materials to facilitate surface diffusion of activated hydrogen species and thus allow secondary hydrogen spillover processes. Hydrogen spillover studies using noble metals and coinage metals supported on several carbon materials have been reported in numerous studies, either for hydrogen storage or in catalytic reactions.[3,11,16] Chung and co-workers,[17] observed an enhanced hydrogen spillover effect on an oxidized Pd/AC (AC, activated carbon) at room temper-ature (low and high pressures) with Pd serving as the activator. This effect was also attributed to the presence of oxygen functional groups found on the carbon material, which are thought to facilitate the mobility of the spilled-over hydrogen atoms over long distances. Lueking and Yang[18] invoked hydrogen spillover to explain the ability of multiwalled carbon nanotubes (MWCNTs) containing residual Ni particles to store significantly more hydrogen (0.65%) than MWCNTs, which had all the Ni removed by hot acid reflux at 200 °C. Their study also suggested that metal−support interactions were important for the spillover process to occur because dry

mixing of the MWCNTs and the catalyst did not improve hydrogen spillover.

Mesoporous hollow carbon spheres (MHCSs) with their hollow morphology and defective carbon structure could be used to study the extent of hydrogen spillover influence on Ru promoted Co Fischer−Tropsch catalysts. In mesoporous hollow carbon spheres, the pores radiate from inside the cavity through the carbon shell to the outer surface of the MHCS providing easy access for small molecules (e.g., H_2 and CO). Thus, loading of initiator and acceptor metals (i.e., ruthenium and cobalt oxide) inside and outside a defective, porous carbon shell could allow for a study of spillover to delineate the effects of the primary and secondary hydrogen spillover processes.[19,20]

We have chosen to investigate the well-known Ru promoted Co reaction to study the hydrogen spillover effect on MHCS supports. In earlier studies, hydrogen spillover processes have been invoked to explain promoter effects in Ru/Co systems.[21,22] An in situ XAS (X-ray absorption spectroscopy) study by Hong et al.,[9] suggested that Ru(IV) ions implanted inside a Co_3O_4 nanoparticle lattice served as a promoter for Co_3O_4 reduction at low temperatures. However, in other studies it has been proposed that Ru nanoparticles, not the ions, were required to be in close proximity to the cobalt oxide particles to effect Ru promotion on Co_3O_4.[23] Recently Sapunov and co-workers,[24] reported spillover of hydrogen from Ru nanoparticles supported on hyper-cross-linked polystyrene to explain and elucidate the kinetics of the D-glucose hydro-genation process.

In this study, hydrogen spillover effects on Co Fischer−Tropsch catalysts using MHCS as a physical barrier, where the initiator (Ru) was loaded inside and outside the MHCS while the acceptor (Co_3O_4) was loaded onto the MHCS (with and without Ru), were investigated. The use of two catalysts, CoRu/MHCS and Ru@MHCS@Co (see Scheme S1 for nomenclature used), made possible a separation of primary and secondary spillover processes.

2. EXPERIMENTAL SECTION

2.1. Sources of Chemicals. Tetraethylorthosilicate (TEOS 98%; Aldrich), cobalt nitrate hexahydrate (Aldrich), octadecyltrimethox-ysilane (C18TMS; Aldrich), ammonia solution (25%; Fluka), hexadecyltrimethylammonium bromide (CTAB; Aldrich), ruthenium chloride (Aldrich), urea (Promark chemicals), ethanol (98%; Merck), toluene (Merck), HF (40%; Associated chemicals), and nitric acid (55%; Merck) were used as received. Deionized water was used in the experiments.

2.2. Synthesis of Modified Stöber Spheres. Silica spheres were made by adding 50 mL of ammonia solution into a solution of water and ethanol (100 and 800 mL, respectively).[20,25] This solution was then stirred at room temperature for 10 min. To this solution was slowly added 75 mL of TEOS, and the mixture was stirred for 6 h to form monodisperse Stöber spheres. CTAB (25 g) and TEOS (12.5 mL) in 250 mL of ethanol were then added into the solution containing the Stöber spheres. A thin silica shell formed on the silica to generate a slightly porous silica composite material (SiO_2) while stirring the solution overnight (12 h) at room temperature. The SiO_2 spheres were then harvested by filtration and dried at 100 °C for 4 h. This was followed by calcination of the material in air at 500 °C for 4 h. This gave a silica yield of approximately 20 g with >90% yield based on the amount of TEOS used.

2.3. Synthesis of 0.2 and 0.5% Ru/SiO_2. Silica spheres (SiO_2; 4 g) prepared above were dispersed in 250 mL of deionized water by ultrasonication. To this mixture was added 0.2 g of urea and 0.8 or 2 mL of 0.1 M $RuCl_3$ solution; the mixture was then sonicated for 30 min. Homogenous deposition precipitation of Ru was performed at 95

°C for 12 h. The product (ca. 0.2% or 0.5% loaded Ru/SiO_2) was then collected by filtration, washed with deionized water, and then dried at 100 °C overnight.

2.4. Synthesis of $Ru/SiO_2@mSiO_2$ and $SiO_2@mSiO_2$.
The Ru/ SiO_2 or SiO_2 (4 g) was dispersed in a water−ethanol solution (50 and 150 mL, respectively) followed by the addition of ammonia solution (3 mL). The mixed solution was then sonicated for 10 min. To this solution was added a mixture of TEOS (5 mL) and C18TMS (1 mL), and the mixture was left stirring for 5 h at room temperature to form a mesoporous silica shell around the SiO_2 or Ru/SiO_2 composites. The resulting product was then collected by filtration, washed with water, and dried at 100 °C for 2 h, followed by calcination in static air at 550 °C for 4 h.

2.5. Synthesis of Ru@MHCS or MHCS.
The $Ru/SiO_2@mSiO_2$ (0.2 or 0.5%) or $SiO_2@mSiO_2$ was placed in a quartz boat inside a horizontal tube furnace, which was heated to 900 °C at 10 °C/min under argon gas (100 mL min^{-1}). When the desired temperature was reached, argon was bubbled through toluene for 2 h to coat the Ru/ $SiO_2@mSiO_2$ or $SiO_2@mSiO_2$ composite with a carbon shell.

HF (10%; 100 mL) was added to the carbon coated $Ru/SiO_2@mSiO_2$ or $SiO_2@mSiO_2$ to remove the template over 12 h. The HF solution was then decanted followed by purification by centrifugation and repeated washing using deionized water followed by drying at 100 °C to give samples that were called 0.2% Ru@MHCS, 0.5% Ru@ MHCS, or MHCS.

2.6. Catalyst Preparation: Loading of Co Nanoparticles.
Cobalt nanoparticles were loaded onto the Ru@MHCS or MHCS using incipient wetness impregnation. $Co(NO_3)_2 \cdot 6H_2O$ (0.741 g) was dissolved in an appropriate volume of 50:50 water and ethanol solvent mixture, and this solution was then impregnated on the carbon support (MHCS or Ru@MHCS; 1 g) and then dried at 40 °C for 12 h. The catalyst was then heated under a flow of nitrogen gas (20 mL min^{-1}) at 100 °C for 2 h followed by further heating at 300 °C for 2 h. To make sure that all the Co was converted to the Co_3O_4 phase, the catalysts were calcined at 210 °C for 2 h under a flow of 5% O_2/Ar gas mixture. The resulting cobalt loading was expected to be 15%. Three catalysts were prepared: Co/MHCS, 0.2%Ru@MHCS@Co (low Ru loading), and 0.5%Ru@MHCS@Co (high Ru loading). A fourth catalyst was made by adding a Co solution mixed with a Ru solution to give a Co loading of 15% and Ru loading of 0.7%; this was called CoRu/MHCS.

2.7. Material Characterization.
TEM analysis was performed on a Tecnai spirit (T12) transmission electron microscope operating at 120 kV. The samples were dispersed in methanol by ultrasonication and loaded onto a copper grid for TEM analysis. The particle size distribution of the materials formed was determined by counting at least 200 randomly selected particles per sample from different TEM images. Gaussian statistics yielded values for the average particle sizes. SEM analysis was performed on a FEI Nova Nanolab 600 FIB/SEM instrument operating at 30 kV. The samples on a carbon tape were coated with a gold−palladium layer before the analysis. EPMA (electron probe microanalysis) was performed using a CAMECA SX5-FE EPMA, equipped with 5 wavelength dispersive X-ray spectroscopy (WDS) detectors and 12 crystals to select X-ray wavelengths for specific elemental compositions. C, Ru, and Co were mapped during the MD process. Elemental mapping was done using a FEG-SEM (CAMECA), a component of the EPMA instrument. The bulk composition of the catalysts was analyzed using a Bruker D2 phaser equipped with a Lynxeye detector, using a Co−Kα (λ = 0.17889 nm) at 30 kV. The scan ranged from 10° to 90° 2θ in 0.0260° steps. TGA was performed with a Perkin-Elmer STA6000 TGA using high purity nitrogen or air as the purge gas and a heating rate of 10 °C min^{-1}. The flow rate of the purge gas was always 20 mL min^{-1}. N_2 adsorption− desorption experiments were conducted at −195 °C using a Micromeritics Tristar 3000 surface area and porosity analyzer. Prior to an experiment, the sample was outgassed at 150 °C for 4 h under nitrogen gas. The BET surface areas were obtained from adsorption data in a relative pressure range from 0.05 to 0.30. The total pore volumes were calculated from the amount of N_2 vapor adsorbed at a relative pressure of 0.99. The pore size distributions were evaluated

from the desorption branches of the isotherms using the Barrett−Joyner−Halenda (BJH) method. The micropore surface area and volume were calculated using t-plot data. TPR experiments were carried out with a Micromeritics Auto Chem II unit. The catalyst (approximately 50 mg) was placed in a quartz tubular reactor, fitted with a thermocouple for continuous temperature measurement. The reactor was heated in a furnace. Prior to the temperature-programmed reduction measurement, the calcined catalysts were flushed with high-purity argon at 200 °C for 30 min, to remove water or impurities, followed by cooling to ambient temperature. Then, 5% H_2/Ar was switched on, and the temperature was raised at a rate of 10 °C min^{-1} from 50 to 850 °C. The gas flow rate through the reactor was controlled by three Brooks mass flow controllers and was always 50 mL min^{-1}. The H_2 consumption (TCD signal) was recorded automatically by a computer. Pulse chemisorption was performed using the Micromeritics Auto Chem II instrument, to compute the number of active sites on the catalysts. The catalyst (ca. 100 mg) was placed in a quartz tubular reactor. The sample was reduced at 350 °C for 2 h under a hydrogen flow of 50 mL min^{-1}. Before injection of the active gas, the sample was purged using helium gas at 350 °C for 1 h, followed by cooling to ambient conditions. Hydrogen chemisorption (assuming a H_2/Co ratio of 2) was then performed at 150 °C using ultrapure hydrogen as the active gas and argon as the carrier gas. O_2 titration was performed using a Micromeritics ASAP 2020 unit after catalyst reduction using high purity hydrogen (50 mL min^{-1}) at 350 °C for 2 h. The samples were cooled to 200 °C and then reoxidized by injecting pulses of high purity oxygen at 200 °C. The extent of reduction was calculated by assuming Co metal was completely converted to Co_3O_4.

In-situ PXRD experiments were performed under 5% H_2/N_2 on a Bruker D8 Advance fitted with an Anton Paar XRK 900 in situ cell. The diffractometer used a sealed copper tube as the X-ray source operating at 40 kV and 40 mA that provided X-rays with a wavelength of 0.15418 nm in a parallel beam geometry. The Rietveld refinement method was used to analyze the PXRD profiles (fresh and spent catalysts) as described in the Supporting Information (section S1). The Co loading on the MHCS was analyzed using an ICP-OES End on Plasma from Spectro Genesis (Kleve, Germany). A catalyst sample (50 mg) was dispersed in a solution of 5 mL of 55% nitric acid and 40 mL of water to dissolve the Co nanoparticles before analysis.

2.8. Evaluation of Fischer−Tropsch Performance.
The Fischer−Tropsch synthesis was performed in a fixed-bed microreactor. A gas cylinder containing a $H_2/CO/N_2$ mixture (~60/30/10 vol %; purity 99.99) was used to supply the reactant gas stream to the catalyst with a specific space velocity of 1800 mL h^{-1} g^{-1}. N_2 was used as an internal standard in order to ensure accurate mass balances. Catalyst (0.5 g, sieved through a 150 μm mesh, without pelletizing) was added to the reactor (resulting catalyst bed ~4 cm in length) and reduced in situ at 350 °C for 2 h under a stream of H_2 (1.5 bar at 50 mL min^{-1}). After reduction, the reactor temperature was decreased to ambient temperature under a hydrogen flow and then heated up to 220 °C under synthesis gas at a pressure of 10 bar. A hot trap placed immediately after the reactor was held at 150 °C in order to collect wax. A second trap kept at ambient temperature was used to collect the oil and water mixture. All gas lines after the reactor were kept at 100 °C. The flow was controlled using a metering valve and measured by a bubble meter. The product stream was analyzed online using two gas chromatographs. A thermal conductivity detector (TCD), equipped with a Porapak Q (1.50 m × 3 mm) packed column, was used to analyze H_2, N_2, and CO, and a flame ionization detector (FID), equipped with a Porapak Q packed column, was used for the analysis of the hydrocarbons online. Gas chromatography calibration and product analysis have been described elsewhere (see Supporting Information for more information).[26]

3. RESULTS AND DISCUSSION

3.1. Catalyst Preparation and Dispersion.
Hollow carbon spheres with a mesoporous structure were prepared with good uniformity by a standard procedure (Figure S1).[20,27]
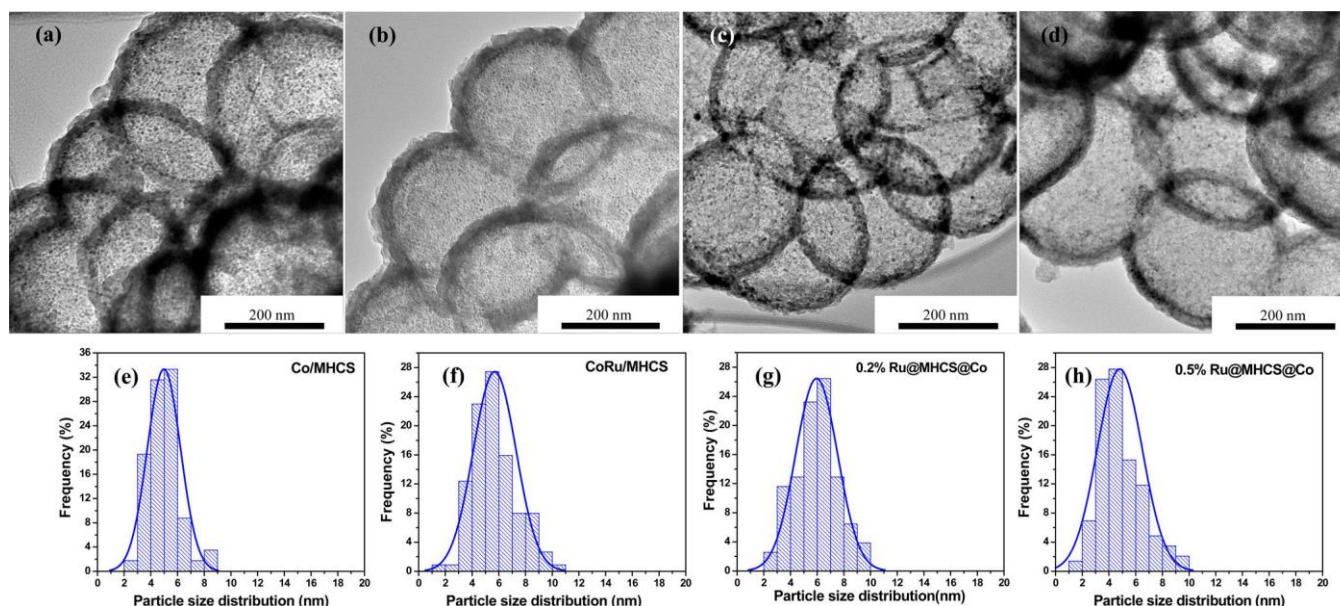
Figure 1. TEM images and particle size distribution of the catalysts: Co/MHCS (a,e), CoRu/MHCS (b,f), 0.2%Ru@MHCS@Co (c,g), and 0.5% Ru@MHCS@Co (d,h).

Ru nanoparticles were placed inside the hollow carbon spheres using a modified method, which was reported in an earlier study.[20] It was important to make a porous carbon shell with short dimensions so as to make sure that the spilled-over hydrogen has a short length to travel on the carbon materials. Hence, the hollow carbon spheres had an average particle diameter of 290 nm (Figure S2) and a carbon shell thickness between 20 and 35 nm (Figure S1). SEM analysis of the hollow carbon spheres confirmed their circular morphology and showed that the majority (>90%) of the MHCS remained intact and were not broken (Figure S1c).[27,28]

The results presented in Figure S1 confirm that both the empty hollow carbon spheres and the hollow carbon spheres containing the Ru nanoparticles inside the spheres have been successfully synthesized. The encapsulation of the Ru nano-particles allowed for physical separation of the Ru from the Co by a layer of mesoporous carbon, making the study of hydrogen spillover effects possible.

Loading of Co nanoparticles (~15%) on both the MHCS and Ru@MHCS was performed by incipient wetness impregnation (IWI) (Figure 1). The Co particle size distributions were obtained from the samples after pretreat-ment in nitrogen and 5% O_2/Ar, and they correspond to the cobalt oxide phase (Co_3O_4). The particle size distribution of the Co_3O_4 nanoparticles for all the catalysts prepared by IWI were in the range of 5−6 nm as determined by transmission electron microscopy analysis (Figure 1 and Table 1)

Catalyst dispersion using EPMA mapping on the 0.2% Ru@MHCS@Co catalyst revealed a homogeneous distribution of Co and Ru on the carbon support (Figure S3). WDS data (Figure S3) also confirmed the complete removal of the silica that was used as the template in the synthesis of the hollow carbon spheres. It should be noted that the Ru nanoparticles inside the MHCS could not be easily observed by TEM because of the carbon shell thickness and density together with the small average particles sizes of the Ru. When the carbon coating step was performed by bubbling Ar through toluene for 1 h (instead of 2 h) to give a thinner and less dense carbon shell, the encapsulated Ru nanoparticles in the 0.5%Ru@

Table 1. Cobalt Content, Particle Size and Pulse Chemisorption Data of the Catalysts

| sample | dispersion (H/Co)[a] | Co_3O_4 particle size (nm) | | Co content (wt %), ICP-OES | Ru content (wt %), TGA |
		TEM	XRD[b]		
Co/ MHCS	0.011	5.3 ± 1.2	4.8	14.6	0
CoRu/ MHCS	0.045	5.6 ± 1.6	4.7	15.4	
0.2%Ru@ MHCS@ Co	0.017	5.9 ± 1.5	4.8	14.1	0.9
0.5%Ru@ MHCS@ Co	0.016	4.8 ± 1.6	4.7	14.8	2.1

[a]Obtained by pulse chemisorption, using a 1:1 ratio of hydrogen atoms to total moles of Co loaded on the sample. [b]Estimated from the Scherrer equation using Rietveld refinement.

MHCS could be readily imaged by TEM (see Figure S1e, d_{Ru} = 4.1 nm).

Pulse chemisorption (Table 1) analysis revealed that the Co metallic dispersion of the catalysts expressed in terms of a ratio of the H atoms adsorbed to Co atoms increased in the order: Co/MHCS < 0.2% Ru@MHCS ≈ 0.5% Ru@MHCS@Co < CoRu/MHCS. This trend was attributed to the increased degree of reduction (i.e., increased number of Co surface sites) due to the intimate contact between the Ru promoter and the Co (on CoRu/MHCS) with more hydrogen adsorbing on the Ru nanoparticles in Ru@MHCS@Co catalysts than on the Co/ MHCS.

3.2. Porosity Analysis Using Nitrogen Adsorption. Porosity analysis of the MHCS and Ru@MHCS with and without Co was performed using nitrogen adsorption−desorption analysis. A typical adsorption isotherm obtained at −195 °C of the materials is included in Figure 2. An analysis of all the isotherms show that the MHCS gave a type IV-like adsorption isotherm as given by the IUPAC guidelines,[29] with
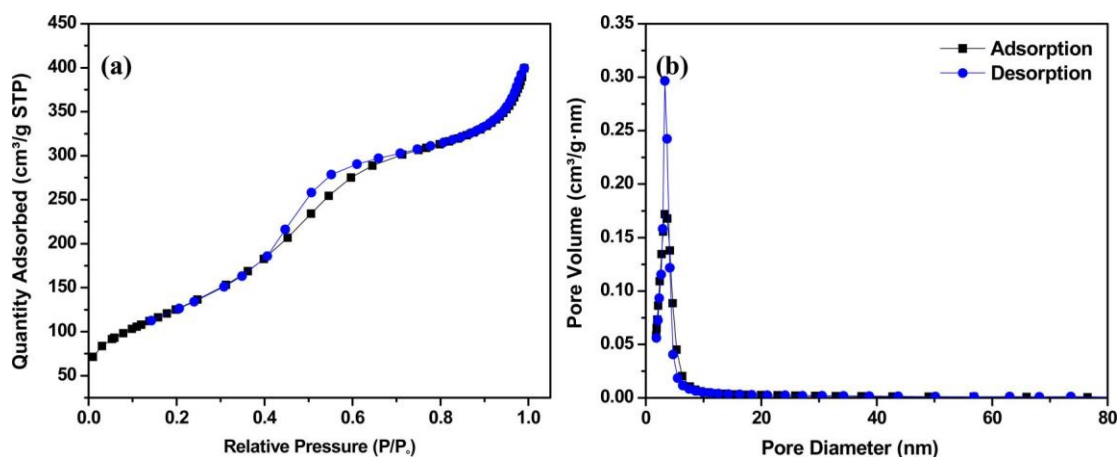
Figure 2. (a) Typical nitrogen adsorption isotherm and (b) BJH pore size distribution of the MHCS and the catalysts (data for Co/MHCS).
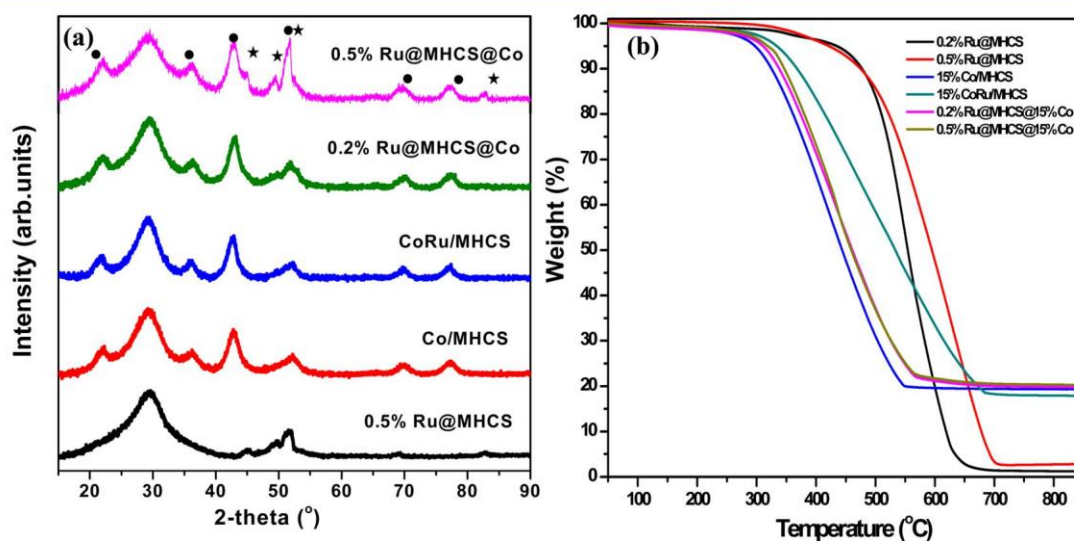

Figure 3. (a) Ex-situ PXRD patterns and (b) TGA profiles of the catalysts. Co_3O_4 (●) and Ru (★).

intertwined mesopores centered around a diameter of 3 nm. This indicated that all the carbon shells were mesoporous regardless of whether there were Ru nanoparticles inside. Co loading on the MHCSs did not significantly affect the carbon shell porosity as illustrated by the corresponding pore size distribution (Figure 2b). It is however noted that introduction of Co nanoparticles on the carbon shell did lower the BET surface area, which can be explained by the blocking of some mesopores by Co_3O_4 nanoparticles thus modifying the carbon shell pore structure (see Figure S4c and Table S1). This can be seen by the appearance of micropores, which made up less than 5% of the total surface area of the Co_3O_4 loaded catalysts (Table S1). All MHCS materials showed high BET surface areas due to the mesoporous carbon shell ($410-480$ m^2 g^{-1}). The mesoporosity of the carbon shell was formed as a result of using the mesoporous silica spheres as a template (sections 2.4 and 2.5), as has also been reported by others.[27,30] The mesoporous silica template displayed a surface area of 165 m^2 g^{-1} in relation to a surface area of 14 m^2 g^{-1} for the unmodified silica spheres (see Table S1 and Figure S4).

3.3. PXRD and TGA. Powder X-ray patterns are shown in Figure 3a, for the catalysts that were obtained after calcination in 5% O$_2$/Ar. The broad distinct peak at 2θ between 28° and 30° is associated with a disordered sp^2 hybridized carbon

structure and was observed for all the catalysts.[31] A cubic cobalt oxide spinel (Co_3O_4) phase was also observed for all the catalysts, as determined by the characteristic peaks that correspond to the Co_3O_4 phase from the ICSD collection file 9362. The broad peaks for the Co_3O_4 phase confirmed that the loaded particles were in the nanoscale range, and they also confirmed a narrow size distribution based on the almost symmetric oxide peak shapes.[32] The supported nanoparticles crystallite sizes were estimated using the Rietveld Refinement to be in the range of $4.7-4.8$ nm (Table 1). This was less than the average particle sizes calculated from TEM images. This is not unexpected as the PXRD estimation has been suggested to always underestimate sizes as it is solely based on the diffracting crystallite planes and not the whole particle.[32] A hexagonal close packed (hcp) Ru phase was observed for the 0.5% Ru@ MHCS and 0.5% Ru@MHCS@Co samples, while Ru in the 0.2%Ru@MHCS was below the detection limit.

Thermogravimetric analysis (Figure 3b) was used to study the thermal stability of the catalysts and the carbon support. The analysis was performed in air, with decomposition of carbon via the oxidation of carbon to CO$_2$. The cobalt oxide nanoparticles catalyze the oxidation of the carbon materials hence lowering the support's decomposition temperature when compared to carbon materials that do not contain cobalt.[33] The
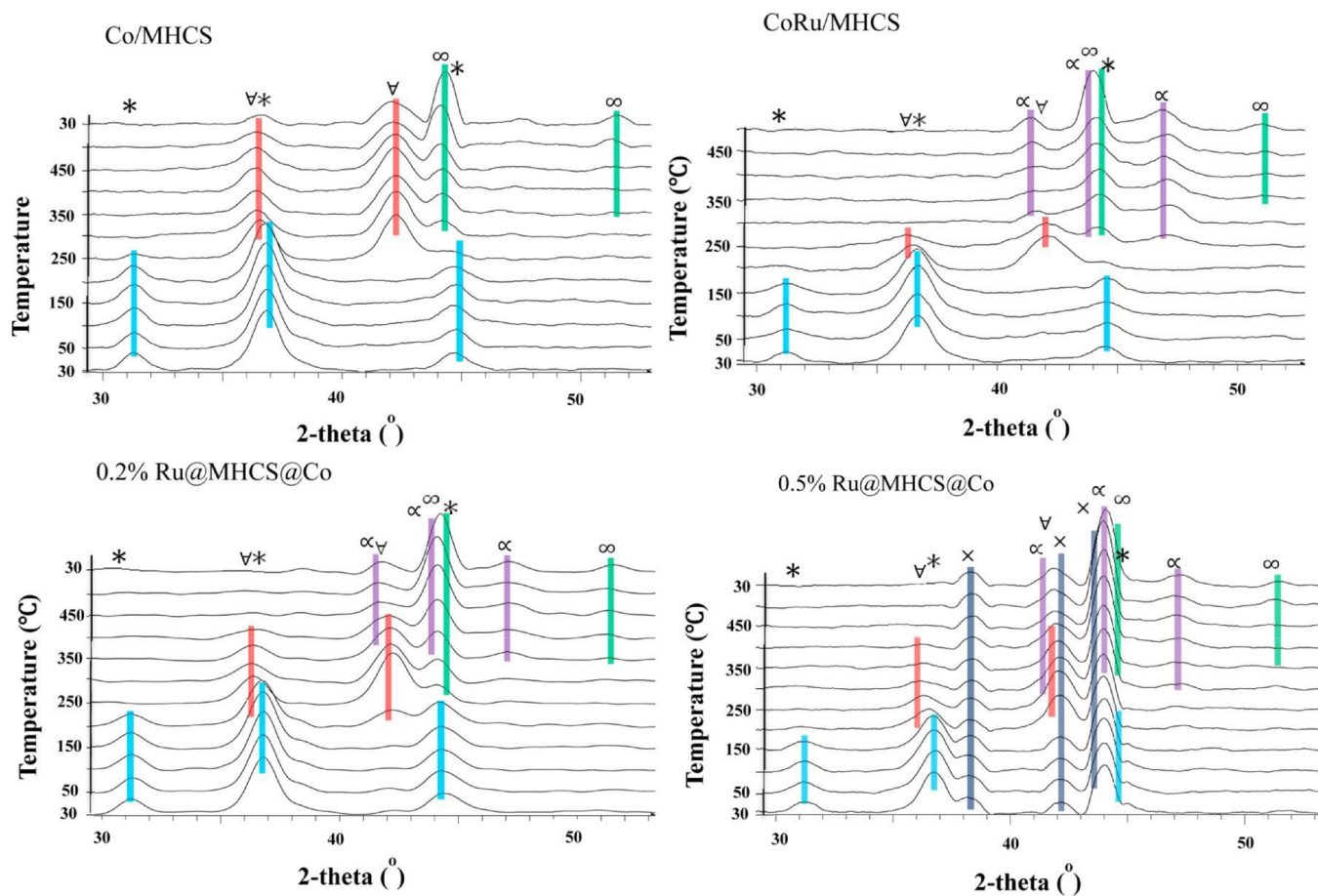
Figure 4. In-situ PXRD profiles of the catalysts under reduction conditions. Co_3O_4 (*), CoO (∀), α-Co (∞), β-Co (α), Ru (×).

onset of carbon decomposition for the Co/MHCS occurred at temperatures above 250 °C while for the carbon materials without Co, support decomposition began at around 410 °C for the 0.2% Ru@MHCS and 0.5% Ru@MHCS samples (Table 1, Figure 3b).

3.4. Reduction of Catalysts: in Situ PXRD. To elucidate the reduction behavior of these Co catalysts an in situ PXRD study was performed. The PXRD patterns were collected at 50 °C intervals under hydrogen gas (Figure 4; for a full pattern see Figure S5).[33−35] The behavior of these catalysts followed the normal reduction for Co_3O_4 with a phase transformation from Co_3O_4 to Co via the CoO intermediate phase. It was however noted that the resulting XRD patterns were influenced by the Ru metal and its location in relation to the Co_3O_4 nanoparticles on the MHCS. For the unpromoted catalyst (Co/MHCS), the Co_3O_4 spinel phase was dominant under the reduction conditions up to 250 °C, and at this temperature, the Co_3O_4 was completely transformed to a CoO phase. At 250 °C, the CoO is dominant with the appearance of a small face centered cubic (fcc or α) Co peak. These two phases (CoO and Co) were observed up to 500 °C with the CoO phase showing a slight decrease in intensity while the fcc Co peak increased in intensity. It was not possible to completely reduce the entire CoO to Co even at 500 °C.

In-situ XRD analysis of the CoRu/MHCS showed that the Co_3O_4 to CoO transition occurred at lower temperature (<200 °C). At 250 °C, both hexagonal close packed (hcp or β) and fcc Co phases were evident together with some CoO. The CoO phase disappeared at temperatures >300 °C. However, the two

metallic Co phases (cubic and hexagonal) were observed up to 500 °C.

In situ analysis of cobalt catalysts in which the Ru nanoparticles were loaded on the inside of mesoporous hollow carbon spheres with different nominal Ru loading (0.2% Ru@ MHCS@Co and 0.5% Ru@MHCS@Co) was also performed. The Co_3O_4 phase transformation for both these catalysts followed a similar trend that was slightly independent of the Ru loading. It should be noted that for the catalysts with a higher Ru loading the Ru phase was detected at all temperatures from

30 to 500 °C. In these two catalysts the Co_3O_4 converted to CoO at 200 °C, and more importantly complete conversion from CoO to Co nanoparticles occurred at temperatures between 400 and 450 °C to form both fcc and hcp Co phases.

The in situ PXRD data (Figure 4) allows us to draw conclusions on the hydrogen spillover from Ru to Co. When Ru is in direct contact with Co on the outside of the MHCS a dominant primary spillover effect is expected. This is supported by the finding that the Co_3O_4 is reduced (i) at low temperature to CoO (<250 °C) and (ii) is completely reduced to fcc and hcp Co 300 °C by the Ru.

Reduction of Co_xO_y is also affected by the relative location of Ru. It is possible that for the Ru@MHCS@Co catalysts, interaction between Co and Ru may take place in the MHCS pores. Incipient wetness impregnation may lead to some Co entering the pores of the hollow carbon spheres; however, the Co particles placed in the pores should still be far removed from the Ru particles when compared to the proximity of the Co and Ru in the CoRu/MHCS catalyst (Figure 5). It is to be
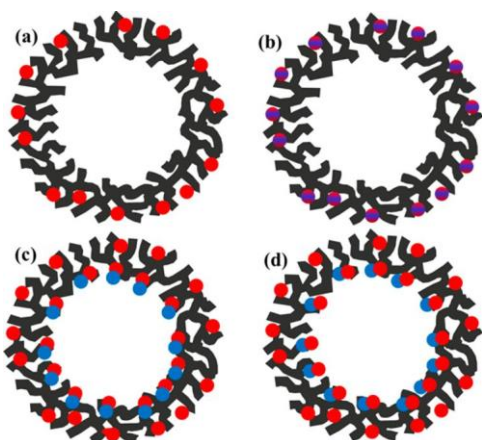
Figure 5. Schematic showing likely Co (red) and Ru (blue) particle distributions on the MHCS support: Co/MHCS (a), CoRu/MHCS (b), 0.2% Ru@MHCS@Co (c) and 0.5% Ru@MHCS@Co (d).

noted that the carbon shell thickness is 20−35 nm and that the pore dimensions are between 3 and 5 nm (Figure 2b). This would suggest that the reduction of the cobalt oxide nanoparticles occurred via a secondary hydrogen spillover effect.

Observations to support a secondary hydrogen spillover effect include the following: (i) the catalysts have similar Co particle sizes, hence the effect of size on the reduction behavior of the Co_3O_4 can be ruled out; (ii) the amount of Ru loading on these two catalysts (0.2% Ru@MHCS@Co and 0.5%Ru@ MHCS@Co) had the expected impact on their reduction

profiles. Thus, the reduction of Co_3O_4 to CoO was complete at temperatures above 200 °C for 0.2% Ru@MHCS@Co and just above 150 °C for 0.5% Ru@MHCS@Co consistent with an expected reduction due to a spillover effect dependent on the amount of Ru loaded; (iii) complete reduction at 450 °C on the Ru@MHCS@Co catalysts, both the hcp and fcc phases were observed to form upon reduction, with the fcc Co appearing at lower temperatures than the hcp Co; however the fcc Co remained the main Co phase. This indicates that the Ru nanoparticles on a carbon support appear to promote initial formation of fcc Co.

The above implies that the Ru promoter effects that are at play on CoRu/MHCS are different from those on Ru@ MHCS@Co and indicates that primary and secondary hydrogen spillover processes can be separated in a Ru promoted Co in carbon support.[36]

Quantitative phase analysis evaluation by Rietveld refinement (using TOPAS 4.2) of the Co phases on the individual PXRD profiles (Figure 6) was used to calculate the relative abundances of the Co species at each temperature.[34] The degree of reduction (DOR) of the catalysts was then estimated as the reduction temperature was increased (Table S3). The estimated DOR at 350 °C was 24% for Co/MHCS, 100% for CoRu/ MHCS, 35% for 0.2% Ru@MHCS@Co, and 44% for 0.5% Ru@MHCS@Co. In contrast the Co/MHCS only gave a DOR of 56% at 500 °C, whereas at this temperature all the other catalysts had a DOR of 100%. The data hence underlines the importance of promoter intimacy for Ru with the Co_3O_4.

The Ru promoted catalysts showed hcp Co to fcc Co ratios to be between 0.1 and 0.3. In the case of Co/MHCS, the
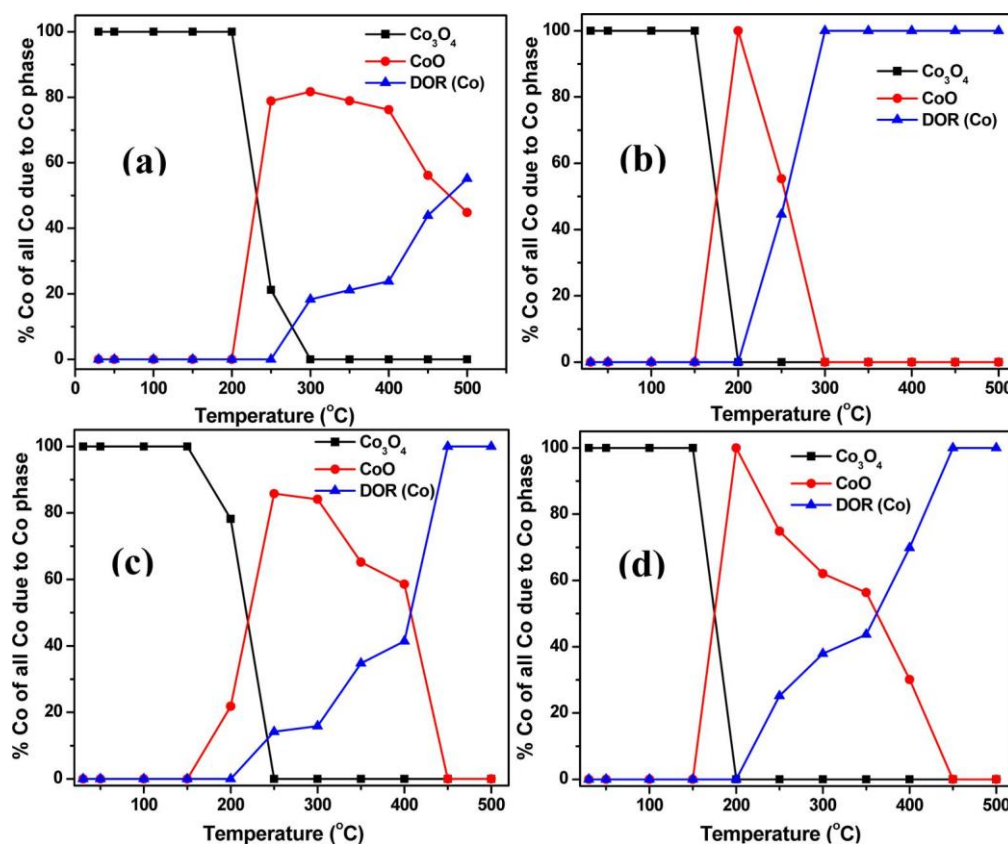

Figure 6. Changes in the Co phase abundance as a function of temperature during in situ PXRD reduction of the catalysts: (a) Co/MHCS, (b) CoRu/MHCS, (c) 0.2% Ru@MHCS@Co, and (d) 0.5% Ru@MHCS@Co.
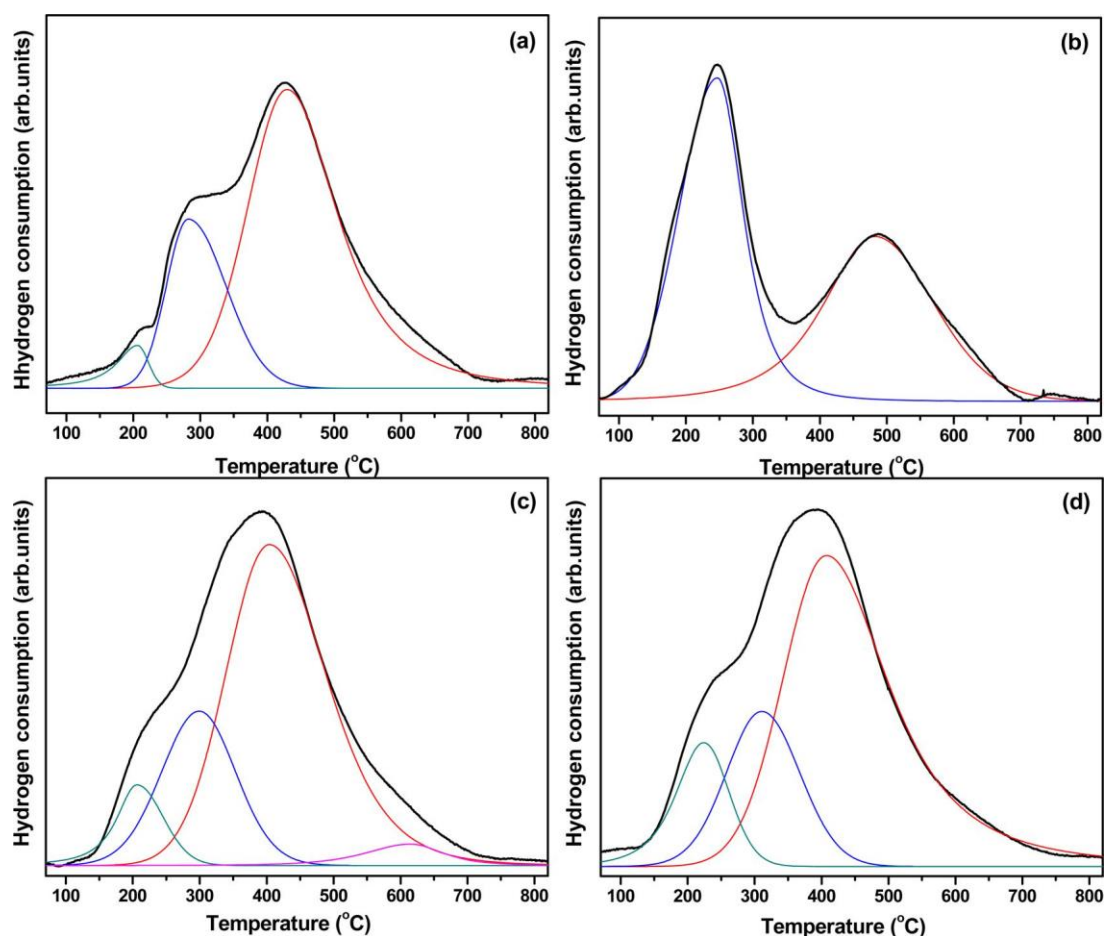
Figure 7. Temperature-programmed reduction profiles of Co/MHCS (a), CoRu/MHCS (b), 0.2% Ru@MHCS@Co (c), and 0.5% Ru@MHCS@ Co (d).

presence of hcp Co from the PXRD patterns was negligible (Figure S6).

The extent of reduction of the catalysts was also determined using oxygen titration after reduction at 350 °C (Figure S7).[37] The reoxidation of the catalysts was performed at 200 °C to avoid carbon support gasification (see TGA plots, Figure S7b). The amount of oxygen consumed was based on the usual assumption that Co nanoparticles would convert to the cobalt oxide spinel phase (Co_3O_4) as supported by XRD analysis of the oxidized catalyst (Figure S7b).

The CoRu/MHCS had the highest degree of reduction (DOR) (90.2%), while the DORs for 0.2% Ru@MHCS@Co and 0.5% Ru@MHCS@Co were 61.5% and 63.2%. Co/MHCS (62.4%) catalysts had lower values. The data are in agreement with the PXRD data recorded at 350 °C shown in Figure S5. The DOR determined using oxygen titration at 350 °C shows that without an intimate Co−Ru contact the reduction of the CoO is less affected by encapsulated Ru nanoparticles.

Thus, primary hydrogen spillover is invoked to explain the reduction of cobalt oxide on CoRu/MHCS, with the electronic effects determining the Co phase that forms during the process (hcp Co when using a carbon support). For the reduction observed on Ru@MHCS@Co catalysts, secondary hydrogen spillover is invoked to explain the complete phase transformation of the cobalt oxide nanoparticles (to Co) that were loaded on the outside of the hollow carbon spheres. Reduction on these catalysts occurred at higher temperatures, and it is most likely that electronic effects for these catalysts were

different from those in CoRu/MHCS. The secondary hydrogen spillover effect requires movement of hydrogen atoms through the carbon shell, which leads to the higher reduction temperatures for the Ru@MHCS@Co catalysts.

3.5. Temperature-Programmed Reduction Studies. The effect of Ru and its location on the reduction of Co_3O_4 particles was further evaluated using temperature-programmed reduction, and the reduction profiles for the four catalysts are shown in Figure 7 (Table S4 shows reduction peak temperatures). After deconvolution, it can be seen that the Co/MHCS and Ru@MHCS@Co catalysts give similar reduction profiles to the reduction of Co_3O_4, but with a shift of the peaks (Table S4). Thus, the stepwise reduction of Co_3O_4 to CoO (ca. 280−310 °C) followed by the reduction of CoO to Co (400−430 °C) was observed.

It should be noted that the addition of a higher loading of Ru on Ru@MHCS@Co results in (i) no significant downward or upward shift of the first reduction peak and (ii) a downward shift of the second reduction peak, when compared to the Co/ MHCS catalyst.

In contrast, when the Ru is placed in close proximity to the Co (CoRu/MHCS), the TPR data are quite different with a shift of the first peak to lower temperatures (247 °C) and a shift of the second reduction peak to higher temperatures (482 °C). A complete reduction of Co_3O_4 consumes one hydrogen molecule for the first reduction process ($Co_3O_4 + H_2 \rightarrow 3CoO + H_2O$) and three hydrogen molecules for the second ($3CoO + 3H_2 \rightarrow 3Co + 3H_2O$). It is then expected that the Co_3O_4

Table 2. Fischer−Tropsch Activity and Selectivity

sample	CO conversion (%)	TOF (10^{-4} s)[a]	activity ×10^{-6} (mol$_{CO}$/g$_{Co}$·s)	selectivity (C mol) (%) C$_1$	C$_2$−C$_4$	C$_{5+}$	α
Co/MHCS	11.2	14.2	5.13	20.1	7.9	72.0	0.81
CoRu/MHCS	19.4	35.9	9.48	23.0	13.3	63.7	0.76
0.2% Ru@MHCS@Co	11.9	17.2	5.15	20.8	9.6	69.6	0.75
0.5%Ru@MHCS@Co	12.4	18.8	5.52	22.4	9.2	68.3	0.74

[a]Calculated using the data obtained from Co crystallite sizes of the spent catalysts as determined by Rietveld refinement (Figure S10 and Table S6). Surface atoms were calculated using the Van Hardeveld and Hartog statistical method.[46]

reduction peaks will be in a ratio of 1:3. However, the peak area ratio of the second reduction peak to the first one was less than one for CoRu/MHCS. This discrepancy can be explained as induced by the Ru promoter, which was in close proximity to the Co oxide nanoparticles. It was therefore assumed that some of the CoO particles were reduced immediately after their formation at the low temperature (247 °C) to form a Co phase to give the higher consumption of hydrogen as seen in the first reduction peak. This is confirmed by the PXRD profiles presented in Figure 4. Other studies have in fact suggested that Ru ions can be doped inside a Co$_3$O$_4$ lattice to assist with the oxide reduction at lower temperatures.[9] The second peak observed at the higher temperature on this catalyst is probably due to gasification of the carbon support, which is catalyzed by the reduced Co nanoparticles (Table S5). Previous studies have shown that at high temperatures, after complete reduction of the cobalt oxide, the gasification of the carbon support ensues and is catalyzed by the reduced Co nanoparticles.[38] Bezemer and co-workers[39] have also suggested that a broad peak at 475 °C in their Mn promoted Co catalysts supported on carbon nanofibers was due to the formation of methane, as was confirmed by gas chromatography analysis. Several other studies support our proposal that the Ru promoter affects Co oxide reduction behavior resulting in a shift of the second reduction peak to low temperatures leading to a possible overlap of the two reduction peaks.[40,41] Irrespective of the exact explanation offered it is clear that placing Ru inside or outside the MHCS leads to substantial changes in the Co oxide reduction behavior.

Reduction profiles in which the Co$_3$O$_4$ nanoparticles and Ru were separated by a carbon shell show that the promoter effects of the Ru were not as prominent as in the catalyst where the two metals are in close proximity (Figure 5c,d). On these catalysts, the first reduction peak occurs at around 300 °C and was not changed by the presence of Ru. However, the second reduction peak was shifted to lower temperatures (~400 °C) relative to the Co/MHCS (429 °C) and suggests that a secondary spillover effect occurs to bring about the complete reduction of CoO to Co on the Ru@MHCS@Co catalysts. The TPR profile of a physical mixture of Co/MHCS and Ru/MHCS showed no discernible shift in the reduction temperature (at 430 °C) of the corresponding CoO to Co phase transformation (Figure S8)

3.6. Fischer−Tropsch Studies. Fischer−Tropsch synthesis over the catalysts was performed at 220 °C at 10 bar pressure for over 100 h on stream (Figure S9). Table 2 shows the Fischer−Tropsch activity and product selectivity of these catalysts. CO conversions of these catalysts were between 10% and 20%. Higher FT activity was observed for CoRu/MHCS at 9.48 × 10^{-6} mol$_{CO}$/g$_{Co}$·s, with a calculated activity almost double that of the other three catalysts that had an activity of about 5 × 10^{-6} mol$_{CO}$/g$_{Co}$·s. However, the two

catalysts with the Ru encapsulated inside the MHCS (i.e., 0.2% Ru@MHCS@Co and 0.5% Ru@MHCS@Co had activities of 5.15 × 10^{-6} and 5.52 × 10^{-6}, respectively) showed a similar or slightly higher activity with respect to the unpromoted catalyst Co/MHCS (5.13 × 10^{-6} mol$_{CO}$/g$_{Co}$·s). The activity of the catalysts can be rationalized based on the reducibility induced by the promoter effects as determined by the Ru metal.[42] The unpromoted catalyst had the lowest FT activity as it had a lower degree of reduction and dispersion of all the catalysts (Table 1 and Table S3). The low turnover frequencies observed for the catalysts were attributed to the small Co crystallites that resulted from the reduction process.[43,44]

In situ PXRD and oxygen titration studies showed that complete reduction of the cobalt oxide on the CoRu/MHCS catalyst occurred at 300 °C and that reduction at 350 °C prior to Fischer−Tropsch reaction ensured a high reducibility. Further, although the Ru@MHCS@Co could also be completely reduced, this occurred at high temperatures (>350 °C). The lower Fischer−Tropsch activity of these catalysts is attributed to their lower degree of reduction because pretreatment of these catalysts by hydrogen reduction prior to Fischer−Tropsch synthesis was performed at 350 °C. The lower number of active sites was confirmed by the pulse chemisorption studies, which showed that Co nanoparticles on CoRu/MHCS displayed a higher catalytic dispersion than the other three catalysts.

Although secondary hydrogen spillover could be invoked to explain the complete reduction of the two encapsulated Ru catalysts, the secondary spillover process did not significantly enhance the degree of reduction of the catalysts at 350 °C. The higher TOF for the CoRu/MHCS promoted catalysts (as compared to Co/MHCS and Ru@MHCS@Co) is related to the high DOR, and the hcp phase which has a higher intrinsic activity for CO hydrogenation reactions than the fcc Co, which was dominant in Co/MHCS.[45]

Fischer−Tropsch activity of the catalysts therefore suggests that primary hydrogen spillover (which gives rise to synergistic electronic effects) is effective in giving a highly active Fischer− Tropsch catalyst, while secondary spillover effects are less effective.

All the catalysts gave methane selectivities of approximately 20 mol %, and the gas phase products C$_2$−C$_4$ were between 7% and 15%, with the C$_{5+}$ selectivities of the catalysts all above 60 mol % carbon. The catalysts with Co and Ru in direct contact (CoRu/MHCS) yielded higher C$_2$−C$_4$ products and lower C$_{5+}$ products. The unpromoted catalyst, Co/MHCS, yielded a higher α value of 0.81, while the promoted catalysts (CoRu/ MHCS, 0.2% Ru@MHCS@Co, and 0.5% Ru@MHCS@Co) had α values calculated to be around 0.75. The high methane selectivities can be accounted for by the small cobalt particle sizes. Several studies have suggested that catalysts with small crystallites give high methane selectivity and that in this size

regime catalytic selectivity is affected by the small Co nanoparticles.[43],[44,47] The Ru promoter did not impact substantially on the catalytic selectivity (when compared to its effect on Fischer−Tropsch activity).[21,22] It can be concluded that the Co particle size played a role in affecting the catalytic activity, but both the primary and secondary spillover effects did not change the catalytic selectivity.

4. CONCLUSIONS

Co Fischer−Tropsch catalysts promoted using Ru metal were prepared using mesoporous hollow carbon spheres (MHCSs) as the support. By preferentially placing Ru nanoparticles inside the MHCSs, it was possible to separate the Co and Ru nanoparticles on the carbon support and to study the effect of primary and secondary hydrogen spillover on Ru promoted Co catalysts during reduction and under Fischer−Tropsch conditions.

It can be concluded that (1) the MHCS was an effective model catalyst support to study the process of primary and secondary hydrogen spillover using Co Fischer−Tropsch catalysts, (2) in-situ PXRD reduction, TPR studies, and a Fischer−Tropsch catalytic evaluation suggested that a greater reducibility at low temperatures and higher Fischer−Tropsch activity could be obtained for catalysts where the Co and Ru metal were in close proximity to each other (CoRu/MHCS), due to a primary hydrogen spillover effect that enhanced cobalt oxide reduction to give a highly active Co catalyst for use in Fischer−Tropsch synthesis, (3) secondary hydrogen spillover was invoked to explain the complete reduction of cobalt oxide on Ru@MHCS@Co where the Co and Ru were separated by a carbon shell, which occurred at relatively high temperatures resulting in a lower degree of reduction when reduced at 350 °C, which could explain the lower Fischer−Tropsch activity, when compared to the CoRu/MHCS, and (4) the catalytic selectivity is correlated with the small Co nanoparticles. The nanoparticles played a significant role in the hydrocarbon product distribution.

■ ASSOCIATED CONTENT

General scheme for synthesis, SEM images of the hollow carbon spheres, EPMA and WDS spectra, adsorption isotherms, Rietveld refinement method, in-situ XRD tables and figures, oxygen titration isotherms and DOR table, FTS CO conversion time on stream and XRD patterns of the spent catalysts (PDF)

■ AUTHOR INFORMATION

Corresponding Author
*Prof Neil Coville. E-mail: neil.coville@wits.ac.za. Tel: +27 (0) 11 717 6738.
Notes
The authors declare no competing financial interest.

■ ACKNOWLEDGMENTS

■ REFERENCES

(1) Jacobs, G.; Das, T. K.; Zhang, Y.; Li, J.; Racoillet, G.; Davis, B. H. Appl. Catal., A 2002, 233 (1), 263−281.
(2) Diehl, F.; Khodakov, A. Y. Oil Gas Sci. Technol. 2009, 64 (1), 11−24.
(3) Beaumont, S. K.; Alayoglu, S.; Specht, C.; Michalak, W. D.; Pushkarev, V. V.; Guo, J.; Kruse, N.; Somorjai, G. A. J. Am. Chem. Soc. 2014, 136 (28), 9898−9901.
(4) Morales, F.; Weckhuysen, B. M. In Catalysis; Spivey, J. J., Dooley, K. M., Eds.; The Royal Society of Chemistry: Cambridge, U.K., 2006; Vol. 19, 1−40.
(5) Choi, M.; Yook, S.; Kim, H. ChemCatChem 2015, 7 (7), 1048−1057.
(6) Nabaho, D.; Niemantsverdriet, J. H.; Claeys, M.; van Steen, E. Catal. Today 2016, 261, 17−27.
(7) Nabaho, D.; Niemantsverdriet, J. W.; Claeys, M.; Steen, E. v. Catal. Today 2016, 275, 27−34.
(8) Storsæter, S.; Tøtdal, B.; Walmsley, J. C.; Tanem, B. S.; Holmen, A. J. Catal. 2005, 236 (1), 139−152.
(9) Hong, J.; Marceau, E.; Khodakov, A. Y.; Gaberová,L.; Griboval-Constant, A.; Girardon, J. S.; Fontaine, C. L.; Briois, V. ACS Catal. 2015, 5 (2), 1273−1282.
(10) Zecevic, J.; Vanbutsele, G.; de Jong, K. P.; Martens, J. A. Nature 2015, 528 (7581), 245−248.
(11) Beaumont, S. K.; Alayoglu, S.; Specht, C.; Kruse, N.; Somorjai, G. A. Nano Lett. 2014, 14 (8), 4792−4796.
(12) Rozanov, V. V. e.; Krylov, O. V. Russ. Chem. Rev. 1997, 66 (2), 107−119.
(13) Im, J.; Shin, H.; Jang, H.; Kim, H.; Choi, M. Nat. Commun. 2014, 5, 3370.
(14) Prins, R. Chem. Rev. 2012, 112 (5), 2714−2738.
(15) Hilmen, A.; Schanke, D.; Holmen, A. Catal. Lett. 1996, 38 (3− 4), 143−147.
(16) Lueking, A. D.; Yang, R. T. Appl. Catal., A 2004, 265 (2), 259−268.
(17) Chung, T. Y.; Tsao, C. S.; Tseng, H. P.; Chen, C. H.; Yu, M. S. J. Colloid Interface Sci. 2015, 441, 98−105.
(18) Lueking, A.; Yang, R. T. J. Catal. 2002, 206 (1), 165−168.
(19) Lee, J.; Kim, S. M.; Lee, I. S. Nano Today 2014, 9 (5), 631−667.
(20) Phaahlamohlaka, T. N.; Kumi, D. O.; Dlamini, M. W.; Jewell, L. L.; Coville, N. J. Catal. Today 2016, 275, 76−83.
(21) Bruce, L. A.; Hoang, M.; Hughes, A. E.; Turney, T. W. Appl. Catal., A 1993, 100 (1), 51−67.
(22) Hoang, M.; Hughes, A. E.; Turney, T. W. Appl. Surf. Sci. 1993, 72 (1), 55−65.
(23) Park, J. Y.; Lee, Y. J.; Karandikar, P. R.; Jun, K. W.; Bae, J. W.; Ha, K. S. J. Mol. Catal. A: Chem. 2011, 344 (1), 153−160.
(24) Sapunov, V. N.; Grigoryev, M. Y.; Sulman, E. M.; Konyaeva, M. B.; Matveeva, V. G. J. Phys. Chem. A 2013, 117 (20), 4073−4083.
(25) Stöber, W.; Fink, A.; Bohn, E. J. Colloid Interface Sci. 1968, 26 (1), 62−69.
(26) Moyo, M. Cobalt and iron supported on carbon spheres catalysts for Fischer−Tropsch synthesis. PhD Thesis, Faculty of Engineering and the Built Environment, University of the Witwatersrand, Johannesburg, 2012.
(27) Nongwe, I.; Bepete, G.; Shaikjee, A.; Ravat, V.; Terfassa, B.; Meijboom, R.; Coville, N. J. Catal. Commun. 2014, 53, 77−82.
(28) Petkovich, N. D.; Stein, A. Chem. Soc. Rev. 2013, 42 (9), 3721−3739.
(29) Gregg, S. J.; Sing, K. S. W.; Salzberg, H. J. Electrochem. Soc. 1967, 114 (11), 279C−279C.
(30) Chen, X.; Kierzek, K.; Wenelska, K.; Cendrowski, K.; Gong, J.; Wen, X.; Tang, T.; Chu, P. K.; Mijowska, E. Chem. - Asian J. 2013, 8 (11), 2627−2633.
(31) Chen, X.; Kierzek, K.; Cendrowski, K.; Pelech, I.; Zhao, X.; Feng, J.; Kalenczuk, R. J.; Tang, T.; Mijowska, E. Colloids Surf., A 2012, 396, 246−250.
(32) Weidenthaler, C. Nanoscale 2011, 3 (3), 792−810.

(33) Dlamini, M. W.; Kumi, D. O.; Phaahlamohlaka, T. N.; Lyadov, A. S.; Billing, D. G.; Jewell, L. L.; Coville, N. J. ChemCatChem 2015, 7 (18), 3000−3011.

(34) du Plessis, H. E.; Forbes, R. P.; Barnard, W.; Erasmus, W. J.; Steuwer, A. Phys. Chem. Chem. Phys. 2013, 15 (28), 11640−11645.

(35) Rayner, M. K.; Billing, D. G.; Coville, N. J. Acta Crystallogr., Sect. B: Struct. Sci., Cryst. Eng. Mater. 2014, 70 (3), 498−509.

(36) Trepanier, M.; Tavasoli, A.; Dalai, A. K.; Abatzoglou, N. Appl. Catal., A 2009, 353 (2), 193−202.

(37) Li, J.; Coville, N. J. Appl. Catal., A 1999, 181 (1), 201−208.

(38) Fu, T.; Jiang, Y.; Lv, J.; Li, Z. Fuel Process. Technol. 2013, 110, 141−149.

(39) Bezemer, G. L.; Radstake, P.; Falke, U.; Oosterbeek, H.; Kuipers, H.; Van Dillen, A.; De Jong, K. J. Catal. 2006, 237 (1), 152− 161.

(40) Coronel-García, M.; de la Torre, A. R.; Melo-Banda, J.; Martínez-Salazar, A.; Rodrigo, R. S.; Zavala, N. D.; Martínez, B. P.; Domínguez, J. Int. J. Hydrogen Energy 2015, 40 (48), 17264−17271.

(41) Jermwongratanachai, T.; Jacobs, G.; Shafer, W. D.; Pendyala, V. R. R.; Ma, W.; Gnanamani, M. K.; Hopps, S.; Thomas, G. A.; Kitiyanan, B.; Khalid, S.; Davis, B. H. Catal. Today 2014, 228, 15−21.

(42) Kogelbauer, A.; Goodwin, J. G., Jr.; Oukaci, R. J. Catal. 1996, 160 (1), 125−133.

(43) Den Breejen, J.; Radstake, P.; Bezemer, G.; Bitter, J.; Frøseth, V.; Holmen, A.; Jong, K. d. J. Am. Chem. Soc. 2009, 131 (20), 7197− 7203.

(44) Fischer, N.; Van Steen, E.; Claeys, M. J. Catal. 2013, 299, 67− 80.

(45) Liu, J. X.; Su, H. Y.; Sun, D. P.; Zhang, B.-Y.; Li, W. X. J. Am. Chem. Soc. 2013, 135 (44), 16284−16287.

(46) Van Hardeveld, R.; Hartog, F. Surf. Sci. 1969, 15 (2), 189−230.

(47) Bezemer, G. L.; Bitter, J. H.; Kuipers, H. P.; Oosterbeek, H.; Holewijn, J. E.; Xu, X.; Kapteijn, F.; van Dillen, A. J.; de Jong, K. P. J. Am. Chem. Soc. 2006, 128 (12), 3956−3964.